

Automatic Segmentation and Visualization of Choroid in OCT with Knowledge Infused Deep Learning

Huihong Zhang, Jianlong Yang*, Kang Zhou, Liyang Fang, Fei Li, Yan Hu, Yitian Zhao, Xiulan Zhang, and Jiang Liu

Abstract—The choroid provides oxygen and nourishment to the outer retina thus is related to the pathology of various ocular diseases. Optical coherence tomography (OCT) is advantageous in visualizing and quantifying the choroid *in vivo*, because it does not suffer from the information contamination of the outer retina in fundus photography and scanning laser ophthalmoscopy and the resolution deficiency in ocular ultrasound. However, its application in the study of the choroid is still limited for two reasons. (1) The lower boundary of the choroid (choroid-sclera interface) in OCT is fuzzy, which makes the automatic segmentation difficult and inaccurate. (2) The visualization of the choroid is hindered by the vessel shadows from the superficial layers of the outer retina. In this paper, we propose to incorporate medical and imaging prior knowledge with deep learning to address these two problems. We propose a biomarker infused global-to-local network, for the choroid segmentation. It leverages the thickness of the choroid layer, which is a primary biomarker in clinic, as a constraint to improve the segmentation accuracy. We also design a global-to-local strategy in the choroid segmentation: a global module is used to segment all the retinal layers simultaneously for suppressing overfitting, then a local module is used to refine the segmentation with the biomarker infusion. The U-shape convolutional network is employed as the backbone in these modules. For eliminating the retinal vessel shadows, we propose a deep learning pipeline, which firstly use anatomical and OCT imaging knowledge to locate the shadows using their projection on the retinal pigment epithelium layer, then the contents of the choroidal vasculature at the shadow locations are predicted with an edge-to-texture two-stage generative adversarial inpainting network. The experiments shows the proposed method outperforms the existing methods on both the segmentation and shadow elimination tasks on a OCT dataset including 1280 labeled OCT B-scans and 136 OCT volumes. We further apply the proposed method in a clinical prospective study for understanding the pathology of glaucoma, which demonstrates its capacity in detecting the structure and vascular changes of the choroid related to the elevation of intra-ocular pressure.

Index Terms—choroid, optical coherence tomography, vasculature, glaucoma

This work was supported by Ningbo 2025 S&T Megaprojects, Zhejiang Provincial Natural Science Foundation (LQ19H180001), and Ningbo Public Welfare Science and Technology Project (2018C50049).

H. Zhang, J. Yang, L. Fang, Y. Zhao are with Cixi Institute of Biomedical Engineering, Chinese Academy of Sciences, China. (*corresponds to yangjianlong@nimte.ac.cn)

F. Li and X. Zhang are with State Key Laboratory of Ophthalmology, Zhongshan Ophthalmic Center, Sun Yat-sen University, China.

K. Zhou is with School of Information Science and Technology, ShanghaiTech University, China.

Y. Hu and J. Liu are with Department of computer science and engineering, Southern University of Science and Technology, China.

H. Zhang is also with University of Chinese Academy of Sciences, China.

I. INTRODUCTION

The choroid, lying between the retina and the sclera, is the vascular layer which provides oxygen and nourishment to the outer retina [1]. Because traditional imaging modalities like fundus photography and scanning laser ophthalmoscopy acquire 2D overlapping information of the outer retina and the choroid, the pathological changes of the choroid could not be precisely retrieved and evaluated. On the other hand, ocular ultrasound is able to do 3D imaging, but it needs to touch the eye and has a low spatial resolution.

Optical coherence tomography (OCT) is a high-resolution non-invasive 3D imaging modality that could precisely separate the information of the underlying choroid from the outer retina, thus has been becoming a powerful tool to understand the role of the choroid in various ocular diseases [2]. It has been shown that the thickness of the choroid layer extracted from OCT, is directly related to the incidence and severity of predominate ocular diseases, such as pathological myopia [3], diabetic retinopathy (DR) [4], age-related macular degeneration (AMD) [5], and glaucoma [6].

Besides, the choroidal vasculature has also been applied in the study and diagnosis of ocular diseases. Agrawal *et al.* found the choroidal vascularity index, which is extracted from binarized OCT B-scan, is related the vascular status of DR [7]. The choroidal vessel density (CVD), extracted from binarized *en face* choroid image, has been used in the

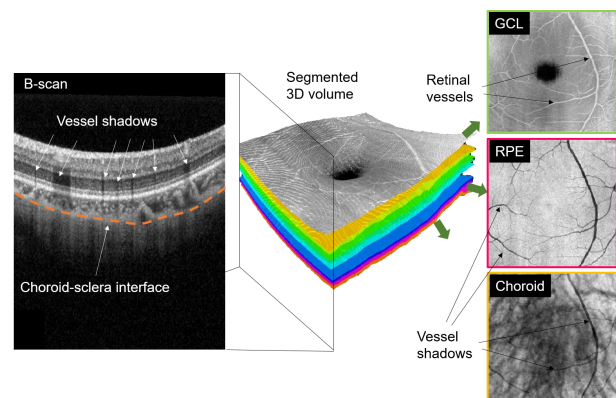


Fig. 1. Demonstration of the choroid-sclera interface (orange dashed line) and the retinal vessels and their projection (arrows) on the underlying layers including the GCL (green box), RPE (pink box) and choroidal vasculature (orange box). GCL: ganglion cell layer. RPE: retinal pigment epithelium.

evaluation of AMD [8] and central serous chorioretinopathy [9]. Wang *et al.* further introduced the choroidal vascular volume, which combines the CVD and the choroidal thickness, is more sensitive in detecting proliferative DR [10].

However, the application of the choroidal biomarkers in clinic is still quite limited, which may be attributed to two primary reasons. (1) The lower boundary of the choroid (choroid-sclera interface, CSI) in OCT is fuzzy, which makes the automatic segmentation difficult and inaccurate. (2) The visualization of the choroid is contaminated by the vessel shadows from the superficial layers of the outer retina.

Figure 1 is a demonstration of the CSI and the retinal vessels and their projection on the underlying layers. The position above the orange dashed line shows the fuzzy CSI in a B-scan. The anisotropy of the red blood cells inside the vessels cause strong forward attenuation of the probe light, thus bring shadow-like dark tails to the underneath layers extending to the choroid and the sclera (white arrow). The center part of Fig. 1 is a segmented OCT volume, which could further be used to generate the en face images of each layer in the right side. The ganglion cell layer (GCL) possesses the retinal vessels (black arrows) and has high light reflectance (green box). The depth-projected vessel shadows (black arrows) turn dark on the vessel-absent retinal pigment epithelium (RPE) layer (pink box) and the choroid layer (orange box). It is evident that the shadows bring difficulties to the extraction of the choroidal vasculature.

Due to their clinical significance, the automatic segmentation and visualization of the choroid have drawn numerous research interests recently [11]–[17]. However, the majority of the choroid segmentation methods are based on graph search [18], which is restricted by the choice of a suitable graph-edge weight model [15]. The inferior choice of the edge weight or the variation of OCT image features would cause inaccuracy in the choroid segmentation [19], so tedious manual inspection and correction are still required for clinical usage [20]. The existing methods for eliminating the vessel shadows are based on the compensation of vessel-induced light attenuation [21], [22], but the effectiveness of this kind of A-line based method is limited to small vessels and capillaries in OCT retinal imaging. The large vessel shadows still have residue on the choroid [23].

To address these two problems, and inspired by the recent success of deep learning in medical image processing [24], [25], we propose an automatic segmentation and visualization method for the choroid in OCT via knowledge infused deep learning. The main contributions of our work include:

- We propose a biomarker infused global-to-local network, for the choroid segmentation. It leverages the thickness of the choroid layer, which is a primary biomarker in clinic, as a constraint to improve the segmentation accuracy.
- We design a global-to-local strategy in the choroid segmentation: a global module is used to segment all the retinal layers simultaneously for suppressing overfitting, then a local module is used to refine the segmentation with the biomarker infusion.
- For eliminating the retinal vessel shadows, we propose a

deep learning pipeline, which firstly locate the shadows using their projection on the retinal pigment epithelium layer, then the contents of the choroidal vasculature at the shadow locations are predicted with an edge-to-texture generative adversarial inpainting network.

- The experiments shows the proposed method outperforms the existing methods on both the segmentation and shadow elimination tasks on a OCT dataset including 1280 labeled OCT B-scans and 136 OCT volumes.
- We further apply the proposed method in a clinical prospective study for understanding the pathology of glaucoma, which demonstrates its capacity in detecting the structure and vascular changes of the choroid related to the elevation of intra-ocular pressure (IOP).

The remainders of the paper are organized as follows. We review the existing techniques related to the proposed method in Section II. The methodology of the proposed method is presented in Section III. To validate the effectiveness and clinical significance of the proposed method, we conduct extensive experiments in Section IV. We analyse and discuss the details of the proposed method in Section V, and draw our conclusion in Section VI.

II. RELATED WORKS

1) *Automatic Choroid Segmentation*: The segmentation of the retinal layers in OCT has been explored since the commercialization of spectral domain (SD) OCT [26]–[28], but the segmentation of the choroid layer was usually not included in these studies, which may be attributed to the fussy CSI (as a comparison, the outer retinal layers usually have sharp and smooth boundary as shown in Fig. 1). Hu *et al.* adapted the graph search algorithm to semi-automatically identify the choroidal layer in SD-OCT [11]. Tian *et al.* segmented the CSI by finding the shortest path of the graph formed by valley pixels using Dijkstras algorithm [12]. Alonso *et al.* developed an algorithm that detected the CSI based on OCT image enhancement and a dual brightness probability gradient [13]. Chen *et al.* generated a gradual intensity distance image. Then an improved 2-D graph search method with curve smooth constraints was used to obtain the CSI segmentation [14].

Deep learning techniques have also been used in the segmentation of the choroid. Sui *et al.* combined the graph search with convolutional neural network (CNN) by using the CNN to decide the edge weights in the graph search [15]. Masood *et al.* converted the segmentation tasks into a binary classification task, which extracted the choroid part of OCT images into patches with or without the CSI [16]. The U-shape convolutional network (U-Net) may be the most successful architecture for medical image segmentation to date [29]. Cheng *et al.* proposed an improved U-Net with refinement residual block and channel attention block for the choroid segmentation [17].

2) *Vessel Shadow Elimination in OCT*: In 2011, Girard *et al.* developed an attenuation compensation (AC) algorithm to remove the OCT vessel shadows and enhance the contrast

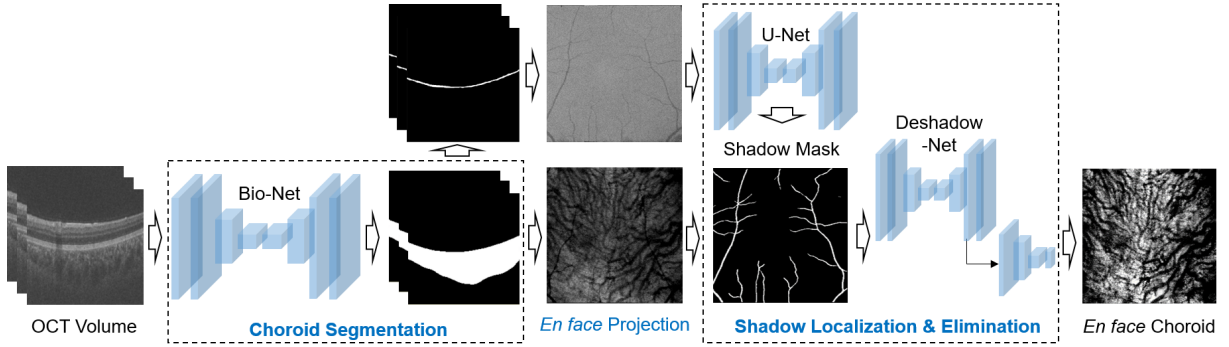


Fig. 2. Illustration of the framework of our method, which primarily includes the choroid segmentation using the proposed Bio-Net, *en face* projection, and the shadow localization and elimination using the U-Net for shadow location mask generation and the Dshadow-Net for shadow elimination. The choroid layer of a OCT volume is firstly segmented by the Bio-Net. We also can get the RPE layer by moving the upper boundary of the choroid $20\ \mu\text{m}$ upward. Then the OCT volume is projected into the 2D *en face* plane with the mean value projection along the axial direction, for generating the *en face* RPE and choroid images. The vessel shadows in the RPE image is segmented with the U-Net to locate their positions. Finally, the shadow location mask in combination with the *en face* choroid image are inputted into the Dshadow-Net for the shadow elimination.

of optic nerve head [21]. This algorithm was then employed in the calculation of the attenuation coefficients of retinal tissue [30], enhancing the visibility of lamina cribrosa [31], and improving the contrast of the choroid vasculature and the visibility of the sclera-choroid interface [32], [33].

Very recently, Mao *et al.* analysed the energy profile in each A-line and automatically compensated the pixel intensity of locations underneath the detected blood vessel [22]. However, both of these methods perform well for the removal of small vessel shadows but unable to handle the large vessel shadows, which would lead to shadow residue on the choroid [23].

3) *Inpainting/Object Removal*: After locating the vessel shadows, we propose to use inpainting techniques, which is also referred as object removal. Here the object to be removed is the vessel shadows. Inpainting techniques have been extensively studied and applied in various computer vision and pattern recognition related fields (see [34], [35] and the references therein). Early inpainting techniques primarily filled the targeted area with information from similar or closest image parts, such as exemplar-based inpainting (EBI) [36], or used higher-order partial differential equations to propagate the information of surrounding areas into the targeted area, such as coherence transport inpainting (CTI) [37].

Deep learning, especially generative adversarial network (GAN) [38], is a powerful tool for image synthesis [39], which has also shown its superiority in image inpainting [40]–[42]. Yeh *et al.* used a GAN model to search for the closest encoding of the corrupted image in the latent image manifold using context and prior losses, then passed the encoding through the GAN model to infer the missing content [40]. Yu *et al.* utilized contextual attention on surrounding image features as references during GAN training to make better predictions [41]. Nazeri *et al.* proposed a two-stage GAN inpainting method, which comprises of an edge generator followed by an image completion network. The edge generator hallucinates edges of the missing region of the image, and the image completion network fills in the missing regions using hallucinated edges as a priori [42].

III. METHODOLOGY

Figure 2 is an illustration of the framework of our method, which primarily includes the choroid segmentation using the proposed Bio-Net, *en face* projection, and the proposed shadow localization and elimination pipeline. We use the U-Net for shadow location mask generation and the Dshadow-Net for shadow elimination. The Dshadow-Net follows the architecture of the two-stage inpainting GAN in [42]. The choroid layer of a OCT volume is firstly segmented by the Bio-Net. We also can get the RPE layer by moving the upper boundary of the choroid $20\ \mu\text{m}$ upward. Then the OCT volume is projected into the 2D *en face* plane with the mean value projection along the axial direction, for generating the *en face* RPE and choroid images. The vessel shadows in the RPE image is segmented with the U-Net to locate their positions. Finally, the shadow location mask in combination with the *en face* choroid image are inputted into the Dshadow-Net for the shadow elimination.

A. Bio-Net for Choroid Segmentation

As shown in Fig. 3, the Bio-Net is a cascade of biomarker prediction network, global multi-layers segmentation module, and local choroid segmentation module. Firstly, the biomarker prediction network is trained to predict the biomarker, and its parameters are fixed after that. Then, we follows the anatomical hierarchy of the retinal OCT and employ the global multi-layers segmentation module to segment the OCT image into 12 layers. Finally, the global multi-layered result and the original OCT image are concatenated and fed into the local choroid segmentation module to segment the choroid region, where the biomarker information is infused and applied as a regularization.

1) *Biomarker Prediction Network*: We employ the choroidal thickness as a prior knowledge, which has been found to be related to various ocular diseases as mentioned in the Introduction, to assist the segmentation. The choroidal thickness denotes the average distance between the upper boundary (Brucos membrane, BM) and the lower boundary (CSI). The biomarker prediction network trained a thickness

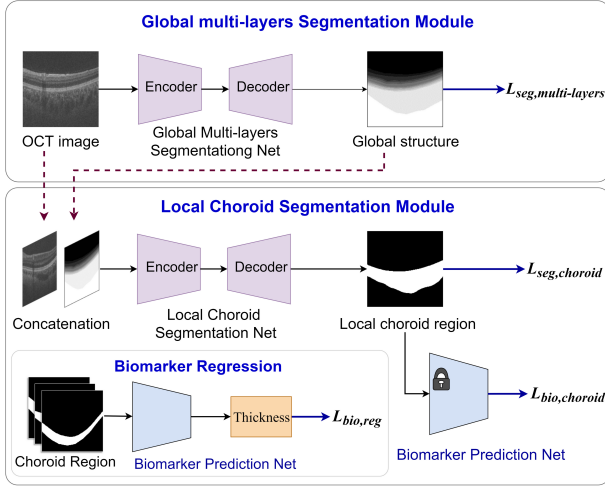


Fig. 3. Illustration of the Bio-Net for the choroid segmentation. Firstly, the biomarker prediction network is trained to predict the biomarker, and its parameters are fixed after that. Then, we follow the anatomical hierarchy of the retinal OCT and employ the global multi-layers segmentation module to segment the OCT image into 12 layers. Finally, the global multi-layered result and the original OCT image are concatenated and fed into the local choroid segmentation module to segment the choroid region, where the biomarker information is infused and applied as a regularization.

regularizer by a set of manually labeled choroid images to learn the distribution of choroidal thickness. Since the upper boundary is easy to detect, the thickness regularizer will be helpful to segment the lower boundary.

The biomarker prediction network \mathbf{B} is trained to predict the biomarker, and the parameters are fixed after that. The biomarker prediction network outputs a vector (x_i, h) for each input, where i denotes the coordinate of the A-line and h is the corresponding predicted thickness. The mean of h is the biomarker value B_{pred} , whose ground-truth is B_{gt} . It is trained with mean absolute error loss, denoted as $L_{bio,reg}$.

$$L_{bio,reg} = \frac{1}{N} \sum_{n=0}^{N-1} \|B_{pred} - B_{gt}\| \quad (1)$$

where n denotes the index of samples, N denotes the total number of samples.

2) *Global Multi-Layers Segmentation Module*: The global multi-layers segmentation module is to segment the global OCT image into several layers following its anatomical characteristics. As a multi-task network, the tasks of segmenting different layers are constrained with each other, which can reduce overfitting and improve robustness. It is trained by a multi-class loss, which aims to optimize the global classification loss. This module is mainly used to obtain the global structure information of the retinal OCT.

The global multi-layers segmentation module takes OCT image I_{input} as input and estimates the global multi-layers result G_{pred} via a segmentation block \mathbf{U}_G , $G_{pred} = \mathbf{U}_G(I_{input})$. We employ the U-Net [29] as the \mathbf{U}_G . G_{gt} denotes the ground truth of the global structure. The G_{gt} is an OCT image with the label of 12 retinal layers. This module is trained with cross

entropy loss. The loss function is calculated as follow:

$$L_{seg, multi-layers} = -\frac{1}{N} \sum_{i=0}^{11} [G_{gt} \ln(G_{pred}) + (1 - G_{gt}) \ln(1 - G_{pred})] \quad (2)$$

where i denotes the index of layers.

3) *Local Choroid Segmentation Module*: The local choroid segmentation module takes the concatenated OCT image and multi-layered result C_{input} as input and predict the choroid region C_{pred} via another segmentation block \mathbf{U}_c , $C_{pred} = \mathbf{U}_c(C_{input})$. It is trained with $L_{seg, choroid}$. When C_{pred} is feed into the biomarker prediction network, it is compared with B_{pred} , then another loss termed $L_{bio, choroid}$ is produced.

$$L_{seg, choroid} = \frac{1}{N} \sum_{i=0}^1 [B_{pred} \ln G_{pred} + (1 - B_{pred}) \ln(1 - G_{pred})] \quad (3)$$

$$L_{bio, choroid} = \frac{1}{N} \sum_{N-1}^{n=0} \|\mathbf{B}(C_{pred}) - B_{pred}\| \quad (4)$$

Finally, the Bio-Net is trained by minimizing the total loss.

$$L_{total} = \lambda_{seg, multi-layers} L_{seg, multi-layers} + \lambda_{seg, choroid} L_{seg, choroid} + \lambda_{bio, choroid} L_{bio, choroid} \quad (5)$$

where $\lambda_{seg, multi-layers}$, $\lambda_{seg, choroid}$, $\lambda_{bio, choroid}$ denote hyper-parameters.

B. Shadow Elimination Pipeline

Different from the previous shadow elimination methods that could not eliminate the shadows from large vessel [21], [22], we propose a novel method that is able to remove the shadow without the limitation in vessel caliber. It firstly locates the shadow without the limitation in vessel caliber. It firstly locates the shadow without the limitation in vessel caliber. It firstly locates the shadow without the limitation in vessel caliber. As shown in Fig. 4, we segment the retinal vessel shadows from the *en face* RPE image with the U-Net [29]. The generated shadow mask could be used to locate the shadows in a OCT volume. Then the shadow mask in combination with the *en face* choroid image are fed into the shadow elimination module, namely the Deshadow-Net, to get a shadow-free choroid image.

1) *Shadow Localization*: The idea of using RPE to locate the vessel shadows is inspired by two medical and imaging knowledge. (1) The retinal layers below the outer plexiform layer and above the BM are avascular [43], so any vessel-like structure appears on these layers are the projected shadows. (2) As shown in Fig. 5, the RPE layer has the highest OCT light reflectance and best shadow contrast compared with other avascular layers including outer nuclear layer (ONL) and photoreceptor layer (PRL).

To fully locate the shadow mask on the *en face* choroid, we further enhance the U-Net segmentation results with morphological manipulation including dilation and erosion.

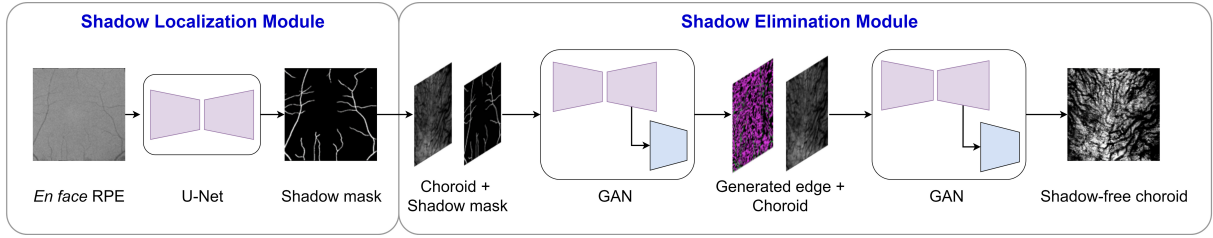


Fig. 4. Illustration of the shadow elimination pipeline. We firstly segment the retinal vessel shadows from the *en face RPE* image with the U-Net [29]. The generated shadow mask could be used to locate the shadows in a OCT volume. Then the shadow mask in combination with the *en face* choroid image are fed into the shadow elimination module, namely the Dshadow-Net, to get a shadow-free choroid image.

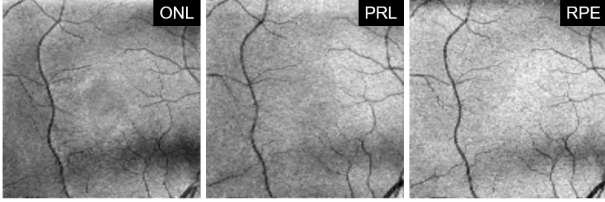


Fig. 5. Comparison of the RPE layer with other avascular layers including outer nuclear layer (ONL) and photoreceptor layer (PRL) in OCT imaging.

2) *Shadow Elimination*: As demonstrated in Fig. 4, the Dshadow-Net is a cascade of two GANs. Each GAN has a pair of generator and discriminator. The generators follow the architecture in [44] and the discriminators use a 70×70 PatchGAN architecture [45]. The inputs of the Dshadow-Net are the shadow-contaminated choroid image and the shadow location mask. Before entering the first GAN, the structure feature of the *en face* choroid is extracted with the Canny edge detector [46]. The first GAN is employed to generate the structure (edge) information in the shadow mask areas. The second GAN uses the edges of the choroidal vasculature generated in the first GAN as a prior, to fill the texture information of the choroid. Then we could get the shadow-free choroid from the output of the second GAN.

IV. EXPERIMENTS

A. Automatic Choroid Segmentation

1) *Dataset*: For the training and testing of the BioNet, we use a dataset named AROD with 256×20 B-scans [47]. Each B-scan has 512 A-lines with 992 pixels in each A-scan. Since the B-scans in the same volume have high similarity, Cheng *et al.* [48] annotates the boundary information for 1/4 of the B-scans, thus $256/4 \times 20 = 1280$ B-scans are used. The 1280 B-scan images were randomly divided into a train set and a test set, each contains 640 B-scans.

Note that the data throughout this paper was collected from Topcon OCT systems, so we did not consider to remedy the domain discrepancy caused by manufacturers in the proposed method. For using it in the scenerios that the OCT systems are from different manufacturers, domain adaptation methods [49], [50] have been used for achieving superior segmentation and shadow elimination performance.

2) *Implementation*: Our Bio-Net is implemented by using PyTorch library [51] in the Ubuntu 16.04 operating system

and the training was performed with NVIDIA GeForce GTX 1080 Ti GPU. We first train the Biomarker Prediction Net to predict the thickness of the B-scan choroid. The backbone is a ResNet18 [52] and it is trained with Adam optimizer with the learning rate of 0.01 and a batch size of 8. The parameters are fixed after that. Then we train the rest of the Bio-Net end-to-end. We utilize flipping and rotation to augment the data. The batch size is 4 and the optimizer is Adam [53]. The initial value of the learning rate is 0.01, and then the learning rate is reduced to 1/10 of the original when the number of iterations is 40, 80, 160, and 240, respectively. We set the hyper-parameter $\lambda_{seg, multi-layers} = 1$, $\lambda_{seg, choroid} = 1$, $\lambda_{bio, choroid} = 0.01$. It took about 4 hours for each training of the Bio-Net.

3) *Evaluation Metrics*: We employ dice index (DI), intersection-over-union (IOU), average-unsigned-surface-detection-error (AUSDE), accuracy (Acc), and sensitivity (Sen) to quantitatively evaluate the performance of the Bio-Net. The DI and IOU show the proportion of the overlap between the segmented choroid region and the ground truth (larger is better). The AUSDE [54] represents the pixel-wise mismatch between the segmented choroid boundary and the ground truth (smaller is better). Acc and Sen represent the accuracy and sensitivity of the segmentation compared with the ground truth (larger is better).

4) *Results*: We compare the BioNet with the existing choroid segmentation methods based on graph search and deep learning. The graph search method use the open source algorithm in [55] and its Matlab implementation¹. The deep learning methods include the U-Net [29], which is the backbone of our Bio-Net, and and the improved U-Net in [17].

Figure 6 shows the visual examples of the choroid segmentation. From left to right are the input OCT B-scans, ground truth, and the segmentation results using the graph search, U-Net, improved U-Net, and our Bio-Net, respectively. As demonstrated in the figure, all of the methods have better performance in the segmentation of the upper choroid bound (the BM) then the lower boundary (the CSI), which may because the BM has bright and sharp features for recognition while the CSI is and dark and fussy. For the CSI segmentation, the graph search method works better in the right side of these B-scan, which may be attributed to the clearer CSI in this side. The deep learning methods generally perform better in the CSI segmentation than the graph search. But the U-Net and improved U-net have local segmentation errors and

¹<https://github.com/javimazzaf/choroidSegmentation>

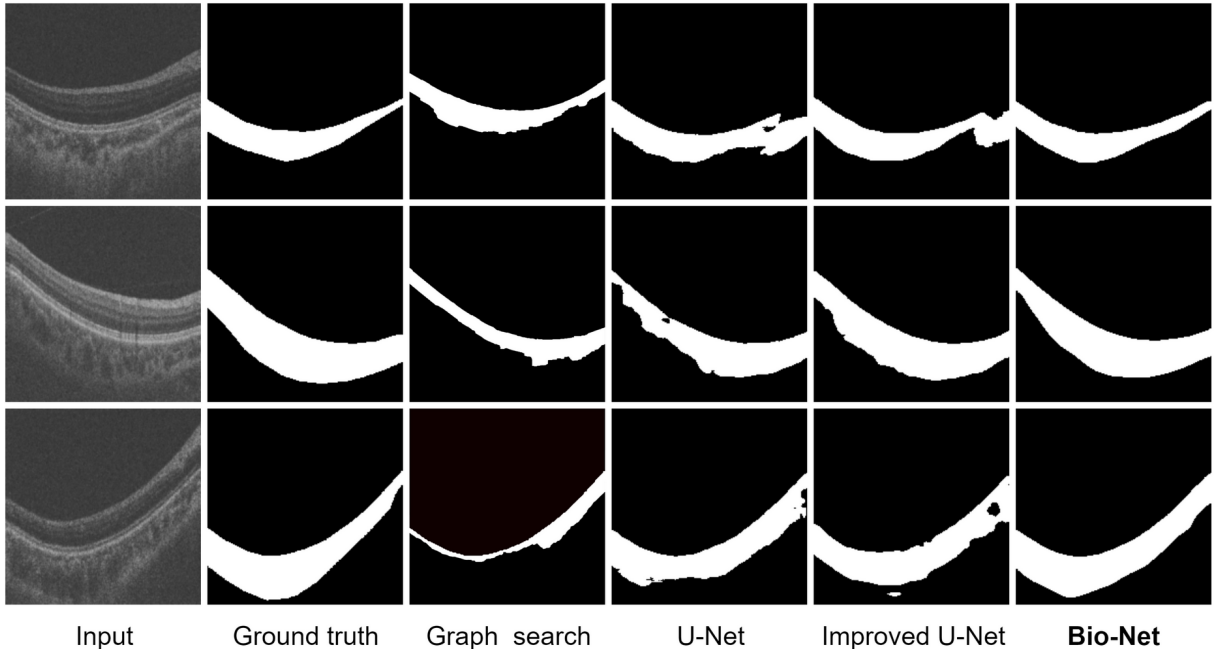


Fig. 6. The visual examples of the choroid segmentation. From left to right: input OCT B-scans, ground truth, and the segmentation results using the graph search [55], U-Net [29], improved U-Net [17], and our Bio-Net, respectively.

discontinuity in both the BM and CSI. The performance degradation in the BM segmentation may suggest the graph search method has better robustness and generalization capacity. On the other hand, because of adding the biomarker knowledge constraint, the proposed method has better consistency in the segmentation of both the CSI and BM and is very close to the ground truth.

Their quantitative comparison is listed in Table I. The

TABLE I
QUANTITATIVE COMPARISON OF DIFFERENT CHOROID SEGMENTATION METHODS ON AROD DATASET.

Method	Metrics				
	IOU	AUSDE	DI	Acc	Sen
Graph Search [55]	45.75	49.04	62.78	86.31	49.04
U-Net [29]	79.14	8.01	88.36	96.30	90.95
Improved U-Net [17]	81.41	6.94	89.75	96.80	90.60
Our Bio-Net	83.10	6.23	90.77	97.14	90.95

performance of deep learning methods is better than the graph search method with the IOU increased by nearly 40%, AUSDE decreased by over 40 pixels, DI increased by nearly 30%, and Sen increased by over 40%. Our Bio-Net outperforms other methods listed in the table with 90.77% DI, 83.10% IOU, 6.23 pixels AUSDE, and 97.14% Acc, which may suggest the infusion of the biomarker prior and the global-to-local strategy contribute to the improvement of the segmentation. We further analyse the quantitative contribution of each innovation in the Discussion Section below.

B. Shadow Localization and Elimination

1) *Dataset*: We employ 30 OCT volumes for the training and testing of the shadow localization and elimination pipeline.

Each volume has $992 \times 512 \times 256$ voxels. They cover a field of view (FOV) of $6 \times 6 \text{ mm}^2$ region and a imaging depth of around 2 mm. We randomly divided these volumes into 25 testing sets and 5 evaluation sets. The choroid and RPE layers of these volumes were segmented with the Bio-Net. Then the *en face* RPE images were manually annotated by two medical experts with pixel-level precision.

2) *Implementation*: The shadow localization and elimination pipeline is also implemented using the PyTorch library [51]. For training the U-Net in the shadow localization, we employ the Adam optimizer [53] for training. The initial learning rate is set to 0.0001. Then we gradually decrease the learning rate with a momentum of 0.9. We further enhance the segmentation result of the U-Net with six iterations of dilation and erosion.

For the shadow elimination, the Dshadow-Net is pre-trained with the neutral scene datasets in [42] then fine-tuned with our choroid datasets. The training of the model is divided into three stages: the edge model, the inpainting model, and the joint model, as suggested in the original implementation².

3) *Evaluation Metrics*: We employ the IOU, Acc, Sen and area under the curve (AUC) to evaluate the segmentation performance of the U-Net. Because no ground truth is available for the shadow elimination task, we employ the vessel density (VD) in the evaluation, which is an indirect but clinically useful metrics. We follow the calculation of the VD in [56] as

$$VD = \frac{\int_A V dA}{\int_A dA}, \quad (6)$$

Where A is the region of interest (ROI). Here it refers to the $6 \times 6 \text{ mm}^2$ centered on fovea. V is the binarized vessel

²<https://github.com/knazeri/edge-connect>

map. For an arbitrary pixel, if it belongs to a vessel, $V = 1$, otherwise $V = 0$.

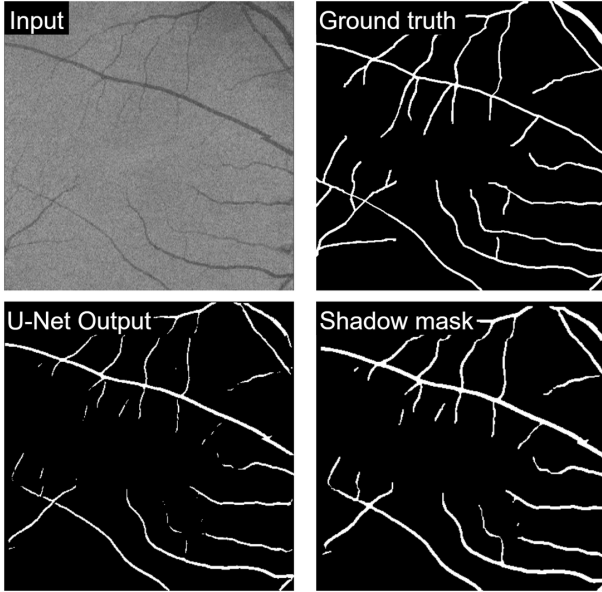


Fig. 7. An example of using the U-Net in the segmentation of the retinal vessel shadows on the RPE image. The U-Net output is further processed to retrieve the shadow mask using dilation and erosion.

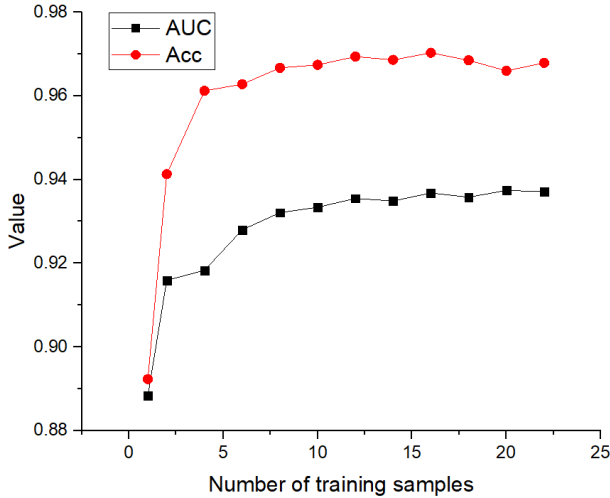


Fig. 8. AUC and Acc values as functions of the number of training samples for the RPE shadow segmentation.

4) *Results*: Figure 7 demonstrates an example of using the U-Net in the segmentation of the retinal vessel shadows on the RPE image. The U-Net output is further processed to retrieve the shadow mask using dilation and erosion. The U-Net achieves superior performance on the vessel shadow segmentation with a Acc of 0.969, a AUC of 0.938, a IoU of 0.901, and a Sen of 0.967. After the dilation and erosion, the vessel caliber is around 5 pixels wider than that of the original shadow, which makes sure the shadow could be completely removed by the Dshadow-Net.

Ronneberger *et al.* have demonstrated the U-Net was capable of achieving excellent segmentation performance with tens

of training samples [29]. Here we found the U-Net could be efficient with less training samples. Figure 8 demonstrates the AUC and Acc values as functions of the number of training samples for the RPE shadow segmentation. As shown in the figure, the AUC and Acc values are close to 0.9 with a single training sample. The two metrics trend to be stable when the number of training images is large than 5, which may be related to the high uniformity of the morphological patterns of the RPE vessel shadows among different OCT volumes.

We compare the proposed shadow elimination pipeline with the A-line based AC algorithm [21] and our previous implementation of this shadow localization and elimination pipeline, which used the CTI as the inpainting algorithm [23]. Figure 9 demonstrates the visual examples of the shadow elimination. From left to right: the original *en face* choroid image, the shadow mask, and the shadow elimination results using different methods. The second and third rows are the zoom-in views inside the blue and yellow boxes in the first row, respectively. The last row are the corresponding vessel maps.

As shown in the figure, the original choroidal vasculature is conterminated by the retinal vessel shadows at the locations shown in the shadow mask. Inside the zoom-in views, the AC could enhance the contrast of the choroidal vessels and minimize small vessel shadows but could not get rid of the large vessel. Using the localization and elimination strategy, both the large and small vessel shadows could be thoroughly eliminated, but as shown in the zoom-in views, the CTI introduces unnatural artefacts compared with the proposed method.

The vessel shadows could be treated as the real vessels in clinical assessment, which would cause the overestimation of the VD. The calculated VD values of the vessel maps in the last row of Fig. 9 are: 0.510 for the original choroid, 0.504 for the AC, 0.501 for the CTI, and 0.500 for the proposed method. We also calculate a VD of 0.499 without including the shadow areas. The results are in accordance with the overestimation assumption, in which the original image has the highest VD. The AC method could eliminate part of the shadows thus lower the VD. The CTI and proposed method could further lower the VD because they remove the shadows completely. Besides, their VDs are very close to that of the masked vessel map, which indicate the effectiveness of this shadow localization and elimination pipeline. We checked the VDs of other testing datasets, which follow the exactly same trend. However, because the variation of the VDs among different eyes are much larger than that of the shadow elimination, we did not include their average values and standard deviations here.

C. Application in a Clinical Prospective Study

Primary angle-closure glaucoma (PACG) is prevailing not only in East Asia but also in overseas Chinese and Eskimos [57]. The patients with PACG were found to have higher IOP and thicker choroids than normal controls [58]. Previous studies shown the changes of the choroid thickness and blood flow might be associated with the PACG [6], but the

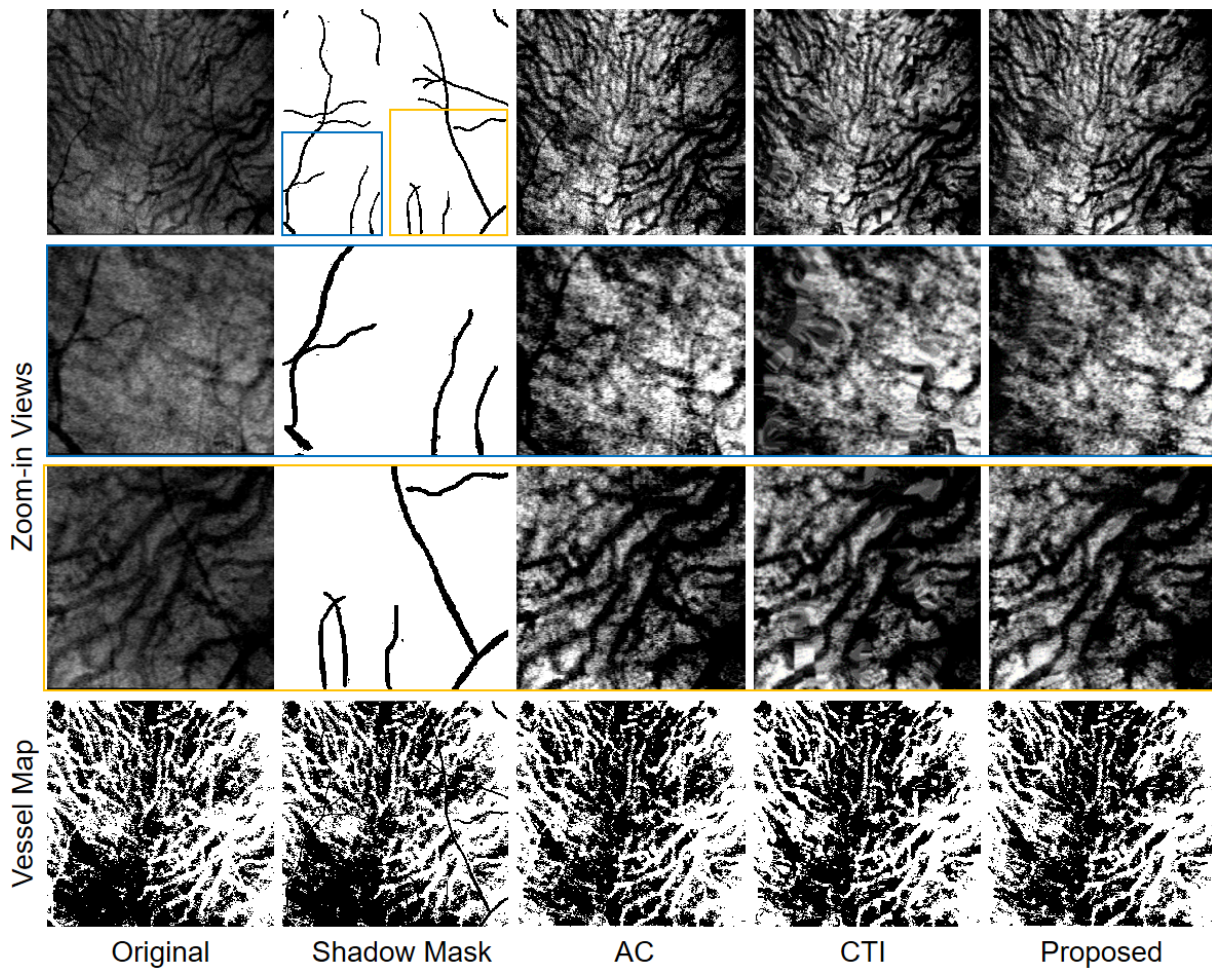


Fig. 9. The visual examples of the shadow elimination. From left to right: the original *en face* choroid image, the shadow mask, and the shadow elimination results using the AC [21], our previous work using the CTI [23], and the proposed method in this work, respectively. The second and third rows are the zoom-in views inside the blue and yellow boxes in the first row, respectively. The last row are the corresponding vessel maps.

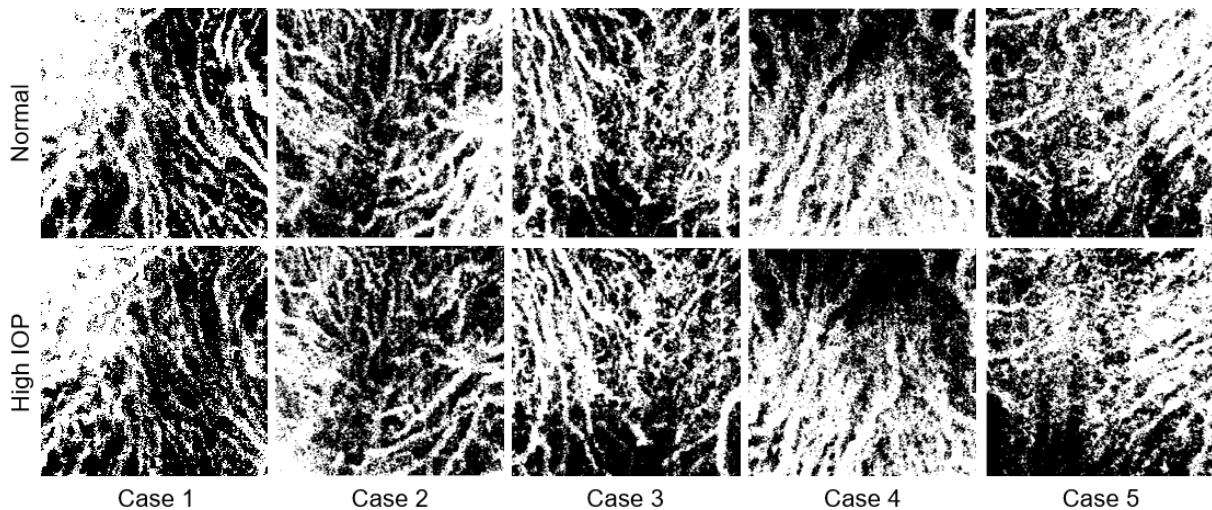


Fig. 10. Demonstration of the vessel maps of 5 study cases in normal (top) and high IOP states (bottom). The reduction in blood flow could be observed in the high IOP state.

initial mechanism underlying angle closure has not been fully understood. Here we applied the proposed method in a clinical prospective study, which quantitatively detected the changes of

the choroidal in response to IOP elevation [20].

1) *Data Collection:* We recruited 34 healthy volunteers with the ages ranging from 18 to 30 years old, with no

previous history of IOP exceeding 21 mm Hg. The participants were volunteers recruited mainly from the Zhongshan Ophthalmic Center at Sun Yat-sen University Medical School, and nearby communities in Guangzhou, China. The study was approved by the Ethical Review Committee of the Zhongshan Ophthalmic Center and was conducted in accordance with the Declaration of Helsinki for research involving human subjects.

A swept-source OCT system with the A-line rate of 100 kHz (DRI OCT-1 Atlantis, Topcon, Japan) was employed to collect data from both of their eyes. We used the 6×6 mm² FOV volumetric scan protocol centered on fovea. Each of the volumes contains 256 B-scans and each of the B-scans has 512 A-lines. Each A-line contains 992 data points uniformly distributed in a depth range of ~ 3 mm.

To simulate the state of high IOP, after taking the baseline scans in a normal sitting position, each of the volunteers was asked to take scans in upside-down position. The average IOP was increased to 34.48 ± 5.35 mm Hg because of the upside-down, compared with the average IOP of 15.84 ± 1.99 mm Hg at the normal position. A total of 136 OCT volumes were acquired (34 volunteers, 68 eyes, normal and high IOP).

2) *Results:* With the proposed knowledge infused deep learning method, we processed this clinical dataset to retrieve the thickness of the choroid and the VD in normal and upside-down states. The choroid thickness is the average value of the 6×6 mm² FOV. We summarize their static averages and standard deviations in Table II.

As the IOP increases from 15.84 ± 1.99 mm Hg during the normal sitting state to 34.48 ± 5.35 mm Hg during the upside-down, the choroid becomes thicker while the VD decreases. Both of them has a p value of < 0.001 . These results provide evidence about the relationship between choroid expansion and

TABLE II
STATICS RESULTS OF THE CLINICAL PERSPECTIVE STUDY

	IOP (mm Hg)	CT [*] (μ m)	VD
Normal	15.84 ± 1.99	226.39 ± 52.44	0.511 ± 0.171
Upside-Down	34.48 ± 5.35	238.34 ± 54.84	0.488 ± 0.164

* CT: choroid thickness.

shallowing of the anterior chamber, which may be of relevance for the pathogenesis of the PACG.

Figure 10 demonstrates the vessel maps of 5 study cases from the clinical dataset in normal (top) and high IOP states (bottom). In OCT imaging, the change on the vessel map is related to the change in blood flow. On these vessel maps, we could observe the reduction in blood flow in the high IOP state.

V. DISCUSSIONS

We further analyse and discuss the details of the proposed method in this section, including the ablation study of the Bio-Net and the comparison of different inpainting methods.

A. Ablation Study of Bio-Net

To evaluate the effectiveness of the global multi-layers segmentation module and the biomarker prediction Net, we combine them with the U-Net respectively.

Table III and Fig. 11 illustrate the effectiveness of the biomarker prediction network and the global multi-layers segmentation module. In the experiment, we take the U-Net as a baseline, the table demonstrates that the infusion of the biomarker prediction network can lead to an improvement on the choroid segmentation task, as the DI increases from

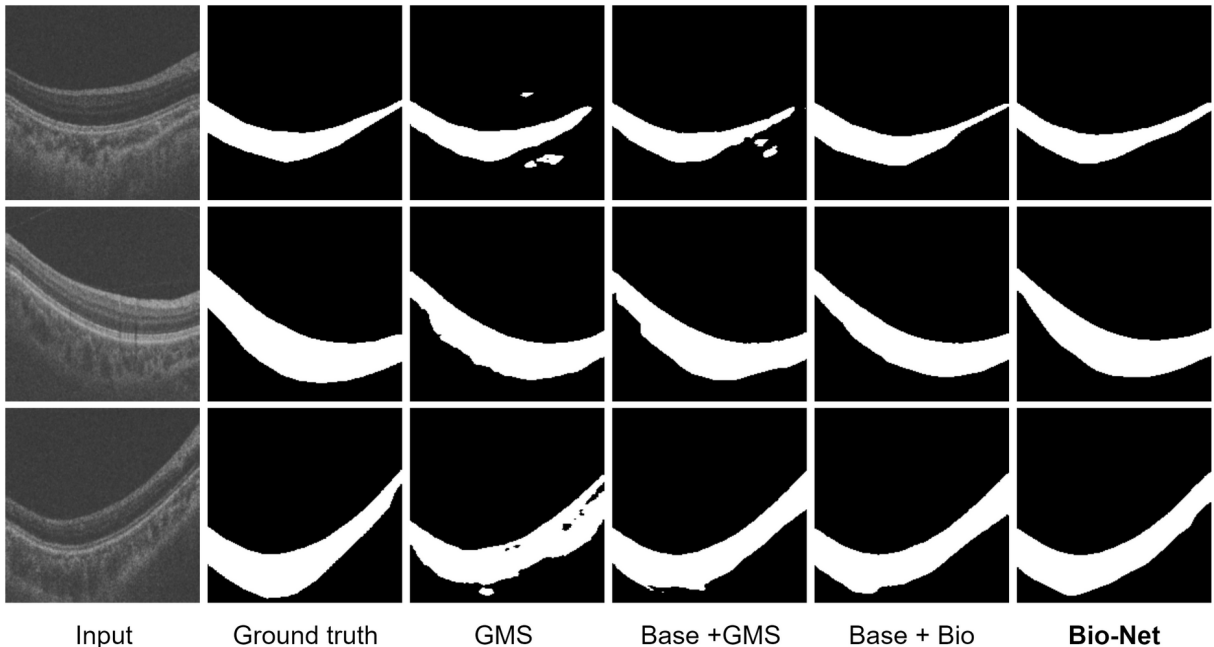


Fig. 11. Ablation study of the Bio-Net. From left to right: the input OCT B-scans, ground truth, the segmentation results using the global multi-layers segmentation module (GMS), the U-Net baseline (base) and the GMS, the baseline and the biomarker constraint (Bio), and our Bio-Net, respectively.

TABLE III
ABLATION STUDY OF THE BIO-NET

Method	Metrics				
	IOU	AUSDE	DI	Acc	Sen
GMS*	79.59	10.04	88.62	96.43	89.79
U-Net+GMS	81.34	6.53	89.71	96.75	91.58
U-Net+Bio**	82.27	6.46	90.27	97.00	89.98
Our Bio-Net	83.10	6.23	90.77	97.14	90.95

* GSM: global segmentation module.

** Bio: biomarker constraint.

88.36% to 90.27% and the AUSDE decreases from 8.01 pixels to 6.46 pixels. On the other hand, the performance of the U-Net added by the global multi-layers segmentation module makes the IOU increases from 79.14% to 81.34% and AUSDE decreases from 8.01 pixels to 6.54 pixels. Meanwhile, the AUSDE is 3.50 pixels lower and Sen 1.79% higher than only GMS module employed, which demonstrates that the global-to-local network works better than a single global multi-layers segmentation module or a single local choroid segmentation module.

B. Quantitative Comparison of inpainting Methods

In this work, we employ the GAN inpainting method [42] for the shadow elimination task. We have compared it with our previous implementation [23] using the CTI [37] as shown in Fig. 9. It shows both of the inpainting methods could completely eliminated the shadows and fill the shadow areas with neutral extensions of surrounding contents. We also could notice the CTI create some locate artefacts. Here we further compare the performance of these inpainting method quantitatively. We also include the EBI [36] in the comparison.

Due to the absent of the ground-truth choroidal vasculature, the quantitative comparison of the inpainting methods can not directly implemented. Thus we created artificial retinal vessel mask with the vessel widths slightly wider than the real shadows. The artificial mask combining with the repaired choroid images were used as the input to evaluate the inpainting algorithms. The widely-used image similarity measures including structure similarity index (SSIM), peak signal to noise ratio (PSNR), and mean squared error (MSE) [48] are employed as quantitative metrics. We used the masked images as the baseline.

As shown in Table IV, the GAN inpainting method outperforms the CTI and EBI methods on all the metrics. However, its advantages are marginal. Because all of the inpainting methods achieve SSIMs > 0.9 , which suggest that all of them could be suitable choice for the proposed localization and elimination pipeline.

VI. CONCLUSION

In this paper, we have developed an automatic method for the segmentation and visualization of the choroid, which combined deep learning networks with prior medical and OCT imaging knowledge. We have proposed the Bio-Net for the choroid segmentation, which is a biomarker infused global-to-local network. It outperforms the state-of-the-art choroid segmentation methods on the AROD dataset. For eliminating

the retinal vessel shadows, we have proposed a deep learning pipeline, which firstly locates the shadows using anatomical and OCT imaging knowledge, then removes the shadow using a two-stage GAN inpainting architecture. Compared with the existing methods, the proposed method has superiority in shadow elimination and morphology preservation. We have further applied the proposed method in a clinical prospective study, which quantitatively detected the changes of the choroid in response to IOP elevation. The results show it is able to detect the structure and vascular changes of the choroid efficiently.

REFERENCES

- [1] D. A. Atchison, G. Smith, and G. Smith, "Optics of the human eye," 2000.
- [2] H. Lavers and H. Zambarkji, "Enhanced depth imaging-oct of the choroid: a review of the current literature," *Graefes Archive for Clinical and Experimental Ophthalmology*, vol. 252, no. 12, pp. 1871–1883, 2014.
- [3] S. Wang, Y. Wang, X. Gao, N. Qian, and Y. Zhuo, "Choroidal thickness and high myopia: a cross-sectional study and meta-analysis," *BMC ophthalmology*, vol. 15, no. 1, p. 70, 2015.
- [4] C. V. Regatieri, L. Branchini, J. Carmody, J. G. Fujimoto, and J. S. Duker, "Choroidal thickness in patients with diabetic retinopathy analyzed by spectral-domain optical coherence tomography," *Retina (Philadelphia, Pa.)*, vol. 32, no. 3, p. 563, 2012.
- [5] G. Yiu, S. J. Chiu, P. A. Petrou, S. Stinnett, N. Sarin, S. Farsiu, E. Y. Chew, W. T. Wong, and C. A. Toth, "Relationship of central choroidal thickness with age-related macular degeneration status," *American journal of ophthalmology*, vol. 159, no. 4, pp. 617–626, 2015.
- [6] S. Chen, W. Wang, X. Gao, Z. Li, W. Huang, X. Li, M. Zhou, and X. Zhang, "Changes in choroidal thickness after trabeculectomy in primary angle closure glaucoma," *Investigative ophthalmology & visual science*, vol. 55, no. 4, pp. 2608–2613, 2014.
- [7] K.-A. Tan, A. Laude, V. Yip, E. Loo, E. P. Wong, and R. Agrawal, "Choroidal vascularity index—a novel optical coherence tomography parameter for disease monitoring in diabetes mellitus?" *Acta ophthalmologica*, vol. 94, no. 7, pp. e612–e616, 2016.
- [8] F. Zheng *et al.*, "Choroidal thickness and choroidal vessel density in nonexudative age-related macular degeneration using swept-source optical coherence tomography imaging," *Investigative Ophthalmology and Visual Science*, vol. 57, no. 14, pp. 6256–6264, 2016.
- [9] Y. Kuroda, S. Ooto, K. Yamashiro, A. Oishi, H. Nakanishi, H. Tamura, N. Ueda-Arakawa, and N. Yoshimura, "Increased choroidal vascularity in central serous chorioretinopathy quantified using swept-source optical coherence tomography," *American journal of ophthalmology*, vol. 169, pp. 199–207, 2016.
- [10] J. C. Wang, I. Laíns, J. Providência, G. W. Armstrong, A. R. Santos, P. Gil, J. Gil, K. E. Talcott, J. H. Marques, J. Figueira *et al.*, "Diabetic choroidopathy: choroidal vascular density and volume in diabetic retinopathy with swept-source optical coherence tomography," *American journal of ophthalmology*, vol. 184, pp. 75–83, 2017.
- [11] Z. Hu, X. Wu, Y. Ouyang, Y. Ouyang, and S. R. Sadda, "Semiautomated segmentation of the choroid in spectral-domain optical coherence tomography volume scans," *Investigative ophthalmology & visual science*, vol. 54, no. 3, pp. 1722–1729, 2013.
- [12] J. Tian, P. Marziliano, M. Baskaran, T. A. Tun, and T. Aung, "Automatic segmentation of the choroid in enhanced depth imaging optical coherence tomography images," *Biomedical optics express*, vol. 4, no. 3, pp. 397–411, 2013.
- [13] D. Alonso-Caneiro, S. A. Read, and M. J. Collins, "Automatic segmentation of choroidal thickness in optical coherence tomography," *Biomedical optics express*, vol. 4, no. 12, pp. 2795–2812, 2013.
- [14] Q. Chen, W. Fan, S. Niu, J. Shi, H. Shen, and S. Yuan, "Automated choroid segmentation based on gradual intensity distance in hd-oct images," *Optics express*, vol. 23, no. 7, pp. 8974–8994, 2015.
- [15] X. Sui, Y. Zheng, B. Wei, H. Bi, J. Wu, X. Pan, Y. Yin, and S. Zhang, "Choroid segmentation from optical coherence tomography with graph-edge weights learned from deep convolutional neural networks," *Neurocomputing*, vol. 237, pp. 332–341, 2017.

TABLE IV
QUANTITATIVE COMPARISON OF DIFFERENT INPAINTING ALGORITHMS

	Masked	EBI [36]	CTI [37]	GAN [42]
SSIM	0.778 ± 0.085	0.901 ± 0.043	0.931 ± 0.015	0.946 ± 0.013
PSNR	11.851 ± 2.605	25.988 ± 3.117	29.352 ± 3.712	30.615 ± 3.824
MSE ($\times 10^3$)	3.464 ± 1.895	0.165 ± 0.092	0.109 ± 0.082	0.091 ± 0.071

- [16] S. Masood, R. Fang, P. Li, H. Li, B. Sheng, A. Mathavan, X. Wang, P. Yang, Q. Wu, J. Qin *et al.*, "Automatic choroid layer segmentation from optical coherence tomography images using deep learning," *Scientific reports*, vol. 9, no. 1, p. 3058, 2019.
- [17] X. Cheng, X. Chen, Y. Ma, W. Zhu, Y. Fan, and F. Shi, "Choroid segmentation in oct images based on improved u-net," in *Medical Imaging 2019: Image Processing*, vol. 10949. International Society for Optics and Photonics, 2019, p. 1094921.
- [18] K. Li, X. Wu, D. Z. Chen, and M. Sonka, "Optimal surface segmentation in volumetric images—a graph-theoretic approach," *IEEE transactions on pattern analysis and machine intelligence*, vol. 28, no. 1, pp. 119–134, 2005.
- [19] S. Lee, N. Fallah, F. Forooghian, A. Ko, K. Pakzad-Vaezi, A. B. Merkur, A. W. Kirker, D. A. Albiani, M. Young, M. V. Sarunic *et al.*, "Comparative analysis of repeatability of manual and automated choroidal thickness measurements in nonneovascular age-related macular degeneration," *Investigative ophthalmology & visual science*, vol. 54, no. 4, pp. 2864–2871, 2013.
- [20] F. Li, H. Li, J. Yang, J. Liu, A. Tin, and X. Zhang, "Upside-down position leads to choroidal expansion and anterior chamber shallowing: Oct study," *British Journal of Ophthalmology*, pp. bjophthalmol–2019, 2019.
- [21] M. J. Girard, N. G. Strouthidis, C. R. Ethier, and J. M. Mari, "Shadow removal and contrast enhancement in optical coherence tomography images of the human optic nerve head," *Investigative ophthalmology & visual science*, vol. 52, no. 10, pp. 7738–7748, 2011.
- [22] Z. Mao, A. Miki, S. Mei, Y. Dong, K. Maruyama, R. Kawasaki, S. Usui, K. Matsushita, K. Nishida, and K. Chan, "Deep learning based noise reduction method for automatic 3d segmentation of the anterior of lamina cribrosa in optical coherence tomography volumetric scans," *Biomedical Optics Express*, vol. 10, no. 11, pp. 5832–5851, 2019.
- [23] J. Yang, X. Mu, Y. Zhao, F. Li, L. Fang, Y. Hu, J. Cheng, X. Zhang, and J. Liu, "Enhancing visibility of choroidal vasculature in oct via attenuation compensation and coherence transport inpainting," *Investigative Ophthalmology & Visual Science*, vol. 60, no. 9, pp. 148–148, 2019.
- [24] D. Shen, G. Wu, and H.-I. Suk, "Deep learning in medical image analysis," *Annual review of biomedical engineering*, vol. 19, pp. 221–248, 2017.
- [25] G. Litjens, T. Kooi, B. E. Bejnordi, A. A. A. Setio, F. Ciompi, M. Ghafoorian, J. A. Van Der Laak, B. Van Ginneken, and C. I. Sánchez, "A survey on deep learning in medical image analysis," *Medical image analysis*, vol. 42, pp. 60–88, 2017.
- [26] M. K. Garvin, M. D. Abramoff, X. Wu, S. R. Russell, T. L. Burns, and M. Sonka, "Automated 3-d intraretinal layer segmentation of macular spectral-domain optical coherence tomography images," *IEEE transactions on medical imaging*, vol. 28, no. 9, pp. 1436–1447, 2009.
- [27] K. Lee, M. Niemeijer, M. K. Garvin, Y. H. Kwon, M. Sonka, and M. D. Abramoff, "Segmentation of the optic disc in 3-d oct scans of the optic nerve head," *IEEE transactions on medical imaging*, vol. 29, no. 1, pp. 159–168, 2009.
- [28] Q. Yang, C. A. Reisman, Z. Wang, Y. Fukuma, M. Hangai, N. Yoshimura, A. Tomidokoro, M. Araie, A. S. Raza, D. C. Hood *et al.*, "Automated layer segmentation of macular oct images using dual-scale gradient information," *Optics express*, vol. 18, no. 20, pp. 21 293–21 307, 2010.
- [29] O. Ronneberger, P. Fischer, and T. Brox, "U-net: Convolutional networks for biomedical image segmentation," in *International Conference on Medical image computing and computer-assisted intervention*. Springer, 2015, pp. 234–241.
- [30] K. Vermeer, J. Mo, J. Weda, H. Lemij, and J. De Boer, "Depth-resolved model-based reconstruction of attenuation coefficients in optical coherence tomography," *Biomedical optics express*, vol. 5, no. 1, pp. 322–337, 2014.
- [31] J. M. Mari, N. G. Strouthidis, S. C. Park, and M. J. Girard, "Enhancement of lamina cribrosa visibility in optical coherence tomography images using adaptive compensation," *Investigative ophthalmology & visual science*, vol. 54, no. 3, pp. 2238–2247, 2013.
- [32] H. Zhou, Z. Chu, Q. Zhang, Y. Dai, G. Gregori, P. J. Rosenfeld, and R. K. Wang, "Attenuation correction assisted automatic segmentation for assessing choroidal thickness and vasculature with swept-source oct," *Biomedical optics express*, vol. 9, no. 12, pp. 6067–6080, 2018.
- [33] K. K. Vupparaboina, K. K. Dansingani, A. Goud, M. A. Rasheed, F. Jawed, S. Jana, A. Richhariya, K. B. Freund, and J. Chhablani, "Quantitative shadow compensated optical coherence tomography of choroidal vasculature," *Scientific reports*, vol. 8, no. 1, p. 6461, 2018.
- [34] C. Guillemot and O. Le Meur, "Image inpainting: Overview and recent advances," *IEEE signal processing magazine*, vol. 31, no. 1, pp. 127–144, 2013.
- [35] O. Elharrouss, N. Almaadeed, S. Al-Maadeed, and Y. Akbari, "Image inpainting: A review," *Neural Processing Letters*, pp. 1–22, 2019.
- [36] A. Criminisi, P. Pérez, and K. Toyama, "Region filling and object removal by exemplar-based image inpainting," *IEEE Transactions on image processing*, vol. 13, no. 9, pp. 1200–1212, 2004.
- [37] F. Bornemann and T. März, "Fast image inpainting based on coherence transport," *Journal of Mathematical Imaging and Vision*, vol. 28, no. 3, pp. 259–278, 2007.
- [38] I. Goodfellow, J. Pouget-Abadie, M. Mirza, B. Xu, D. Warde-Farley, S. Ozair, A. Courville, and Y. Bengio, "Generative adversarial nets," in *Advances in neural information processing systems*, 2014, pp. 2672–2680.
- [39] J.-Y. Zhu, T. Park, P. Isola, and A. A. Efros, "Unpaired image-to-image translation using cycle-consistent adversarial networks," in *Proceedings of the IEEE international conference on computer vision*, 2017, pp. 2223–2232.
- [40] R. A. Yeh, C. Chen, T. Yian Lim, A. G. Schwing, M. Hasegawa-Johnson, and M. N. Do, "Semantic image inpainting with deep generative models," in *Proceedings of the IEEE Conference on Computer Vision and Pattern Recognition*, 2017, pp. 5485–5493.
- [41] J. Yu, Z. Lin, J. Yang, X. Shen, X. Lu, and T. S. Huang, "Generative image inpainting with contextual attention," in *Proceedings of the IEEE Conference on Computer Vision and Pattern Recognition*, 2018, pp. 5505–5514.
- [42] K. Nazeri, E. Ng, T. Joseph, F. Qureshi, and M. Ebrahimi, "Edgeconnect: Generative image inpainting with adversarial edge learning," *International Conference on Computer Vision Workshops*, 2019.
- [43] J. Campbell, M. Zhang, T. Hwang, S. Bailey, D. Wilson, Y. Jia, and D. Huang, "Detailed vascular anatomy of the human retina by projection-resolved optical coherence tomography angiography," *Scientific reports*, vol. 7, p. 42201, 2017.
- [44] J. Johnson, A. Alahi, and L. Fei-Fei, "Perceptual losses for real-time style transfer and super-resolution," in *European conference on computer vision*. Springer, 2016, pp. 694–711.
- [45] P. Isola, J.-Y. Zhu, T. Zhou, and A. A. Efros, "Image-to-image translation with conditional adversarial networks," in *Proceedings of the IEEE conference on computer vision and pattern recognition*, 2017, pp. 1125–1134.
- [46] J. Canny, "A computational approach to edge detection," *IEEE Transactions on pattern analysis and machine intelligence*, no. 6, pp. 679–698, 1986.
- [47] Z. Gu, J. Cheng, H. Fu, K. Zhou, H. Hao, Y. Zhao, T. Zhang, S. Gao, and J. Liu, "Ce-net: Context encoder network for 2d medical image segmentation," *IEEE transactions on medical imaging*, 2019.
- [48] J. Cheng, D. Tao, Y. Quan, D. W. K. Wong, G. C. M. Cheung, M. Akiba, and J. Liu, "Speckle reduction in 3d optical coherence tomography of retina by a-scan reconstruction," *IEEE transactions on medical imaging*, vol. 35, no. 10, pp. 2270–2279, 2016.
- [49] Z. Chai, K. Zhou, J. Yang, Y. Ma, Z. Chen, S. Gao, and J. Liu, "Perceptual-assisted adversarial adaptation for choroid segmentation in optical coherence tomography," *arXiv preprint arXiv:1910.10316*, 2019.
- [50] F. Mahmood, R. Chen, and N. J. Durr, "Unsupervised reverse domain adaptation for synthetic medical images via adversarial training," *IEEE transactions on medical imaging*, vol. 37, no. 12, pp. 2572–2581, 2018.
- [51] A. Paszke, S. Gross, F. Massa, A. Lerer, J. Bradbury, G. Chanan, T. Killeen, Z. Lin, N. Gimelshein, L. Antiga *et al.*, "Pytorch: An

- imperative style, high-performance deep learning library,” in *Advances in Neural Information Processing Systems*, 2019, pp. 8024–8035.
- [52] K. He, X. Zhang, S. Ren, and J. Sun, “Deep residual learning for image recognition,” in *Proceedings of the IEEE conference on computer vision and pattern recognition*, 2016, pp. 770–778.
- [53] D. P. Kingma and J. Ba, “Adam: A method for stochastic optimization,” *arXiv preprint arXiv:1412.6980*, 2014.
- [54] D. Xiang, H. Tian, X. Yang, F. Shi, W. Zhu, H. Chen, and X. Chen, “Automatic segmentation of retinal layer in oct images with choroidal neovascularization,” *IEEE Transactions on Image Processing*, vol. 27, no. 12, pp. 5880–5891, 2018.
- [55] J. Mazzaferri, L. Beaton, G. Hounye, D. N. Sayah, and S. Costantino, “Open-source algorithm for automatic choroid segmentation of oct volume reconstructions,” *Scientific reports*, vol. 7, p. 42112, 2017.
- [56] Y. Jia, J. C. Morrison, J. Tokayer, O. Tan, L. Lombardi, B. Baumann, C. D. Lu, W. Choi, J. G. Fujimoto, and D. Huang, “Quantitative oct angiography of optic nerve head blood flow,” *Biomedical optics express*, vol. 3, no. 12, pp. 3127–3137, 2012.
- [57] J. L. Yip and P. J. Foster, “Ethnic differences in primary angle-closure glaucoma,” *Current opinion in ophthalmology*, vol. 17, no. 2, pp. 175–180, 2006.
- [58] M. Zhou, W. Wang, W. Huang, X. Gao, Z. Li, X. Li, and X. Zhang, “Is increased choroidal thickness association with primary angle closure?” *Acta ophthalmologica*, vol. 92, no. 7, pp. e514–e520, 2014.